Chapter 4

Ni-Sinapic Acid Nanocomposite in the Selective Sensing of Permanganate ions

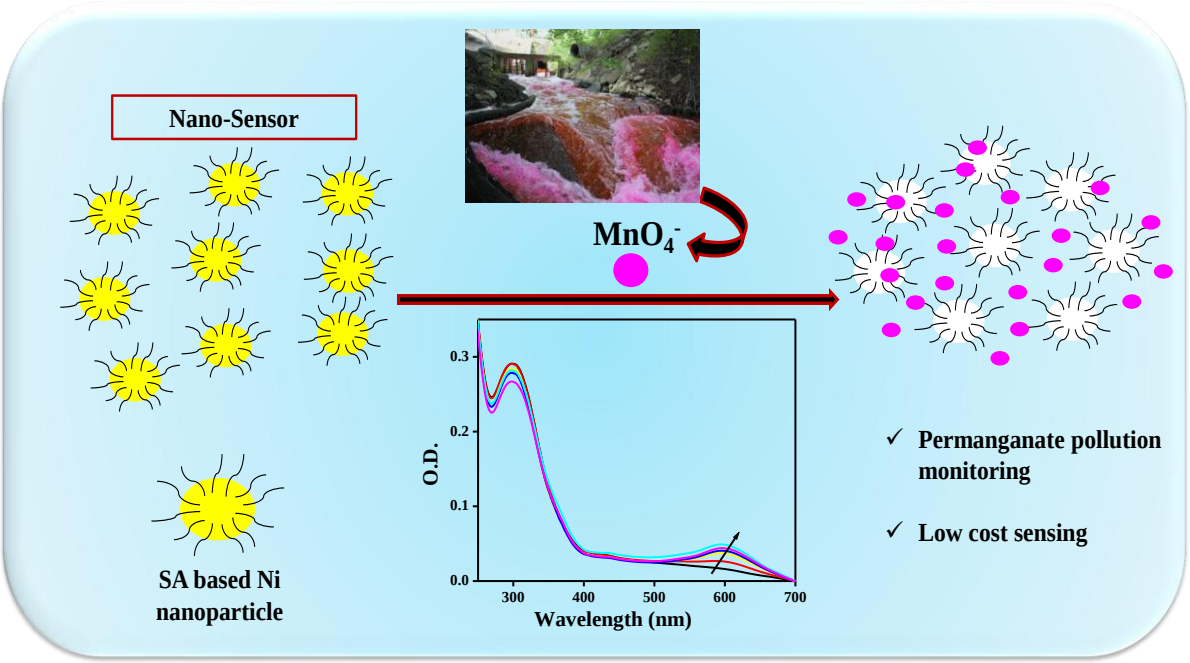

4.1. Introduction

Nanotechnology has become one of vastly growing research fields in the modern science community. In recent years, metals like Fe, Co and Ni have received an immense interest as nanoparticles (NPs) for their beneficial applications in different fields. One of such metal nanoparticles is Ni-based nanoparticles that can be a good semiconductor with their band gap energy in the range 3.6 to 4 eV [Gebretinsae et al., 2021]. Various processes have been utilized to prepare the Ni nanoparticles of different shape and size, which include sol-gel method [Petit et al., 2012], electrodeposition [Golovin et al., 2011], thermal decomposition of organic complexes [Wang et al., 2008], chemical reduction [Ramirez-Meneses et al., 2014], co-precipitation [Sabouri et al., 2018], solvothermal methods [Beach et al., 2009; Anandan et al., 2011], etc. In order to avoid the tedious protocol and the sophisticated instrumentation associated with such methods, green synthesis can be a better option to reduce the use of toxic chemicals and make the process economically more viable [Madhumitha et al., 2016; Mohammadijoo et al., 2014]. One such green methodology to synthesis metal-based nanoparticles is to use plant extract or naturally occurring substances that can act both as capping and reducing agents.

Sinapic acid, a well-known phenolic acid is extensively found in nature, especially vegetables, fruits and a variety of beverages like tea, coffee, etc. It has various pharmacological potentials such as anti-inflammatory, anti-oxidant, anti-bacterial, anti-cancer, anti-anxiety, etc. [Mati et al., 2013; Paul et al., 2011; Ma et al., 2012]. Due to such activities, researchers have paid a great attention to utilise it in developing food, cosmetics and pharmaceutical products. In our recently published paper, we have already shown that sinapic acid also acts as a Cu(II) sensor with a detection limit of 64.5 nM [Sengupta et al., 2018]. Most of the researchers confirmed that the presence of phenolic acids in the plant materials are involved in the reduction and stabilization of metal ions [Sathishkumar et al., 2018].

One of the most important applications of permanganate is its use as an oxidizing agent as the central metal ion (Mn) is in the highest oxidation state [Montomery, 1985]. The reduction potential of MnO_4^-/Mn^{2+} redox couple is 1.51 V in acidic solution. Besides, permanganate is used in water treatment plant [Welch, 1963], treatment of diseases in fish [Wu et al., 2017], washing of vegetables, as an effective sanitary reagent for the reduction of bacterial growth [Subramanya et al., 2018] and so on. On the other hand, Mn(II) is an essential trace element in human body governing the metabolic activity [Lemos et al., 2009; Tu et al., 2019], it can

also be an important constituent for the accurate function of brain, nervous system, enzyme actions, lipid metabolism, growth of bone [Lin et al., 2001; Teo et al., 2001], etc. Dysfunction of central nervous system, neurological disorder, hallucination, mental depression, harmful effects on respiratory, cardiac and reproductive system, problem with DNA mutation, are the most severe consequences of exposure to the excess concentration of Mn(VII) ions. It is therefore important to measure and control the amount of Mn(VII) entering into the body. Adulterated foods often contribute as a major source of Mn(VII) to the human body. At the same time drinking water treated with a requisite amount of Mn(VII), can also be considered as a potential source of this species. WHO has recommended a lower limit of Mn is 9.1 µM in the drinking water [Liu et al., 2019]. Therefore, it is essential to develop an appropriate method to detect Mn(VII) accurately and efficiently in food and water samples. Quite a few number of analytical methods like, spectrophotometry [Lemos et al., 2009], inductively coupled plasma-optical emission spectrometry [Lemos et al., 2009], inductively coupled plasma-mass spectrometry, atomic absorption spectroscopy [Ye et al., 2018], ion chromatography [Ye et al., 2018], etc., are reported in the literature for detection of Mn. But these methods either use toxic solvents or need high temperatures or complicated reagent synthesis or are not sensitive to the oxidation state. In this work, we have used an easy and economically favourable methodology for selective and sensitive detection of permanganate ions in water sample. First we have synthesized sinapic acid based Ni nanoparticle (Ni-SA NPs) in water-ethanol mixed solvent. Then the synthesized nano composite was characterized using different analytical tools like, Fourier transform infrared spectroscopy (FTIR), transmission electron microscopy (TEM), powder X-ray diffraction (PXRD) analysis, etc. It is important to understand the background of the interaction process between $KMnO_4$ and Ni-SA NPs in thermodynamics point of view. Isothermal Titration Calorimetric (ITC) titration was taken up as they provide direct values of ΔH, ΔS as well as stability constant and help to interpret forces of interaction involved [Bhattacharyya et al., 1997; 1997; 1997]. The synthesized nanocomposite was then utilized towards spectrophotometric sensing of permanganate ion in water sample. The method was then further employed for the detection of permanganate ion in natural water samples and in vegetable.

4.2. Materials and Methods

4.2.1. Materials

Sinapic acid (SA) was purchased from Sigma Aldrich, USA. Nickel(II) sulfatehexahydrate ($NiSO_4$. $6H_2O$) (≥98 %) were purchased from Merck, India. Potassium permanganate ($KMnO_4$) (≥99 %), sodium arsenate dibasic heptahydrate ($Na_2HAsO_4.7H_2O$) (99-102 %), sodium chloride (NaCl) (≥99 %), sodium iodide (NaI) (≥99 %), sodium fluoride (NaF) (≥99 %), potassium dichromate ($K_2Cr_2O_7$) (≥99 %), sodium molybdate dehydrate ($Na_2MoO_4.2H_2O$) (≥99 %), sodium peroxidisulfate ($Na_2S_2O_8$) (≥99%), sodium selenate (Na_2SeO_4) (≥99 %), sodium selenite (Na_2SeO_3)(≥99 %), sodium sulfate (Na_2SO_4) (≥99 %), sodium sulfite (Na_2SO_3) (97-100 %), sodium thiosulfate ($Na_2S_2O_3$) (99-100 %) were purchased from Merck, India. Sodium arsenite (Na_3AsO_3) (≥98.5 %) was obtained from S.D. Fine Chem, India. All the required experimental solutions were prepared using triple distilled water. Boring water samples were collected from Garia, Dist.-South 24 parganas, West Bengal, India and from Sonarpur, Dist.- South 24 parganas, West Bengal, India. Tap water sample was collected from Rajabazar, Kolkata, West Bengal, India. Sweet potato was purchased from the local market. All other reagents were of analytical grade and used without further purification.

4.2.2. Apparatus

A powder X-ray diffractometer Rigaku Smart Lab Automatic High Resolution Multipurpose PC Controlled X-Ray Diffractometer System was used for the X-ray diffraction pattern of the nanoparticles. The analysis of functional groups was performed using a Perkin-Elmer L120-00A Fourier Transformed Infrared Spectrometer with sample as KBr pellets. The morphological features of the Ni based NPs was studied using transmission electron microscope (TEM) JEOL JEM 2100 HR with EELS. The planes obtained from the selected area electron diffraction (SAED) pattern of the NP sample have been assigned with the help of imageJ software. UV-Vis spectroscopy was done using Agilent 8453 diode array spectrophotometer and Hitachi UV-Vis U-3501 Spectrophotometer. The change in thermodynamic parameters was examined using Malvern MICROCAL PEAQ-isothermal titration calorimetric (ITC) instrument. A Kratos Axis Ultra DLD system was used to collect X-ray photoelectron spectra (XPS) using monochromatic Al Kα X-ray source operating at 144 W (12 mA × 12 kV).

4.2.3. Synthesis of sinapic acid based Ni-nanoparticles (Ni-SA NPs)

A 10 mM SA solution was prepared in 1:4 ethanol-water mixture of pH~11. A10 mM $NiSO_4$ solution was also prepared in water. Equal amounts of these two solutions were then mixed and kept at 40 °C for 24 hours. The solution was evaporated using an IR-lamp. The residue was washed with 1:4 ethanol-water mixture and collected for further experiment.

4. 3. Characterization

4.3.1. UV-Vis Spectroscopy

After the formation of the NPs, the characterization of the NPs was carried out using absorption spectroscopy. 5 mg of the solid NPs was taken in 0.5 mL of water and then sonnicated for 30 min. This NP solution was then analyzed using UV-Vis spectrophotometer and then compared with the spectra obtained for pure sinapic acid.

UV-Vis spectroscopy was further applied for the sensing study. 2 mL of water was taken in a quartz cuvette and treated with measured aliquots of the NP-solution. Different examined analytes of definite volume was then added to this solution and the results were analyzed using UV-Vis spectroscopy.

4.3.2. Fourier Transform Infrared Spectroscopy (FTIR)

The bond vibrations of the NPs were determined using FTIR analysis. Using a mortar-pestle, a small amount of the solid NPs was thoroughly mixed with dry KBr. The sample was then pelletized using a hydraulic press at a pressure of around 5 ton. The pellet was then placed in the analyzer instrument's sample holder.

4.3.3. Transmission Electron Microscopy (TEM)

The sample for TEM analysis was obtained after dissolving 2 mg of Ni-SA NPs in 2 mL of water-alcohol (1:1) combination and sonication for 1 hour. The dispersed solution was then dropped on a Cu grid with carbon coating. The grid was dried under an IR lamp prior to TEM imaging.

4.3.4. Powder X-ray Diffraction Analysis (PXRD)

The crystalline nature of the produced NPs was determined using powder XRD. Before the X-ray crystallographic study, the powder sample was placed on a rectangular glass holder and then introduced in front of the X-ray.

4.3.5. X-ray Photoelectron Spectroscopy (XPS)

XPS data was collected with pass energies of 160 eV for survey spectra, and 40 eV for the high-resolution scans with step sizes of 1 eV and 0.1 eV respectively. Samples were pressed into copper washers attached, using doubled sided Scotch tape (type 665), to a UV-Ozone cleaned glass microscope and pressed flat with a second clean glass slide.

The system was operated in the Hybrid mode, using a combination of magnetic immersion and electrostatic lenses and acquired over an area approximately 300 × 700 μm^2. A magnetically confined low energy electron charge compensation system was used to minimize charging of the sample surface, and all spectra were taken with a 90° take of angle. A base pressure of ~ 1×10^{-9} Torr was maintained during collection of the spectra.

Transmission corrected spectral data was analysed using CasaXPS (v2.3.25) [Fairley et al., 2021] after subtraction of a Shirley background and using modified Wagner sensitivity factors as supplied by the manufacturer. Charge calibration was made to the lowest binding energy component from the fitted C (1s) spectra of each sample, the value of which was taken to be 285 eV.

4.3.6. Sensing Experiment

The sensing experiment was carried out using different anions viz., MnO_4^-, $HAsO_4^{2-}$, AsO_3^{3-}, Cl^-, $Cr_2O_7^{2-}$, F^-, I^-, MoO_4^{2-}, $S_2O_8^{2-}$, SeO_4^{2-}, SeO_3^{2-}, SO_4^{2-}, SO_3^{2-} and $S_2O_3^{2-}$. 5 mg of the solid nano particle was taken in 0.5 mL of water and then sonicated for 30 mins. This solution was called as the nanoparticle solution. Then 20 µL of this solution was taken in 2 mL of water in a cuvette. Finally, this solution was treated with different aliquots of 0.1 mM of different analytes. The results were analyzed using UV-Vis spectroscopy.

4.3.7. Isothermal Titration Calorimetric (ITC) Analysis

Isothermal Titration Calorimetry (ITC) provided information on the thermodynamic parameters arising out of the interaction of MnO_4^- with Ni-SA NPs. 300 µL of the NP solution was taken in the sample cell. 5 mM $KMnO_4$ was taken in the syringe and 2 µL aliquots were gradually added into the cell. During the experiment, deionized water was used as blank. The calorimetric titrations were carried out for 50 mins at 25º C. The molecular interaction between $KMnO_4$ and NPs can be defined by the following thermodynamic equation (equation 1) based on an ITC analysis:

$$\Delta G = \Delta H - T\Delta S \qquad (1)$$

where, ΔG is the change in Gibbs free energy, ΔH is enthalpy change, ΔS is entropy change, and T is the absolute temperature. The binding stoichiometry can also be measured using the ITC experiment.

The value of ΔG can alternatively be calculated using the following equation with the value of the association constant (K_a) (equation 2)

$$\Delta G = -RT\ln K_a \qquad (2)$$

The universal gas constant, R, is used in this equation.

4.3.8. Interference Study

The interference study was carried out using different co-existing ions viz. $HAsO_4^{2-}$, AsO_3^{3-}, CrO_4^{2-}, $Cr_2O_7^{2-}$, ClO_4^-, PO_4^{3-}, SeO_4^{2-}, SeO_3^{2-}, K^+, Mn^{2+}, Cr^{3+} and Fe^{3+} of equimolar concentration (0.003 mM) to that of the permanganate anion. 40 µL of the nano particle solution was taken in 2 mL of water. 60 µL of each of the interfering ions (0.1 mM) were added separately to this solution and then treated with 60 µL of $KMnO_4$ solution (0.1 mM). The sensing ability of the nano particle towards the permanganate ion was then analysed using UV-Vis spectrophotometer.

4.3.9. Analysis of natural samples

Boring water and tap water samples were collected and used as obtained. Sweet potato weighing ~70 g was chopped with a knife and then soaked in 150 mL of distilled water. After 90 min of soaking, the solution was filtered with a Whatmann-42 filter paper. 2 mL of distilled water was treated with 40 µL of nanoparticle solution and then a small aliquot of these sample solutions were individually added and the data were analysed using UV-Vis spectrophotometer. The amount of MnO_4^- ion present in the sample was estimated using a pre-calibrated equation. Recovery percentage was also checked with tap water by addition of small aliquots of the $KMnO_4$ solution of known concentration. The absorbance data were collected at 593 nm and with the help of a suitable calibration plot, the recovery % of $KMnO_4$ was calculated.

4.4. Result and Discussion

4.4.1. Visual observation

Mixing of equimolar concentrations of $NiSO_4$ and sinapic acid solutions causes the light yellow colour of sinapic acid to change into dark brown. This change in color indicates the

synthesis of Ni-sinapic acid (Ni-SA NPs) nanoparticles.

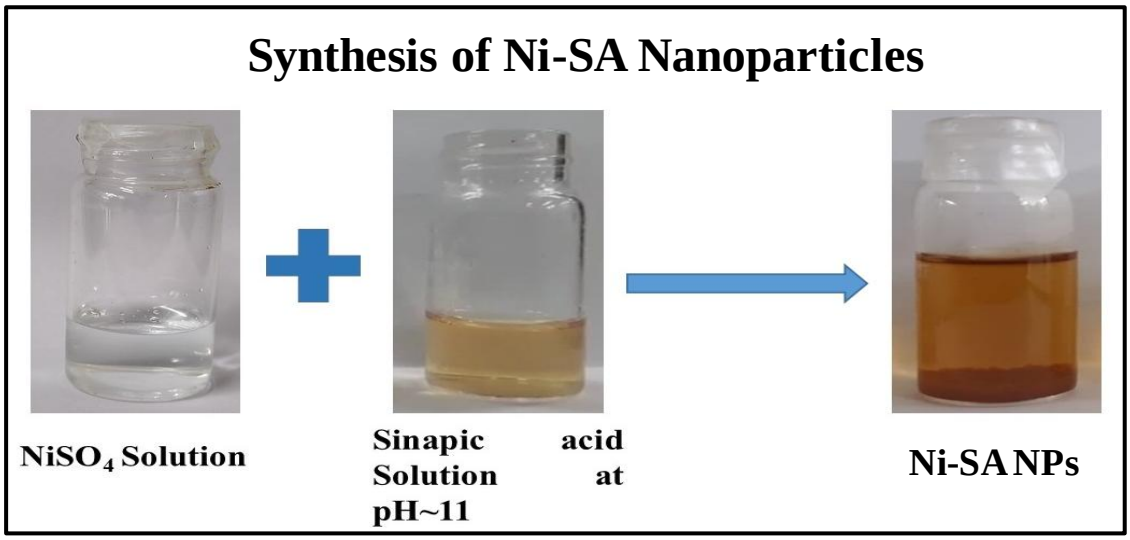

Figure 4.1. The photograph of synthesis of Ni-SA NPs

4.4.2. UV-Vis spectroscopy studies

The formation of Ni-SA NPs was characterized using UV-Vis spectroscopy shown in Fig. 4.2. The characteristic absorption peak of SA (355 nm) at pH~11 disappeared upon formation of the nanocomposite and a new peak appeared at 298 nm. This also indicates that the formation of Ni-SA NPs [Chandra et al., 2014; Hemalatha et al., 2014; Halder et al., 2018].

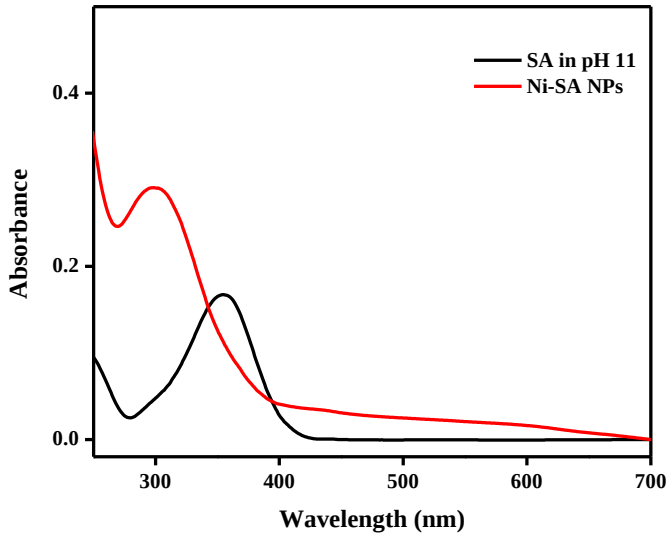

Figure 4.2. UV-Vis spectra of SA and Ni-SA NPs

4.4.3. FTIR analysis

Due to the interaction between the $NiSO_4$ and sinapic acid, a major shift in the IR frequency was observed as compared to the pure sinapic acid. Fig. 4.3 shows three relevant regions: region (a) around 3500-2400 cm^{-1}, region (b) around 1800-1000 cm^{-1}, and region (c) around 1000-500 cm^{-1}.

Region (a) was developed mainly due to the hydroxyl group and -CH_3 group. Region (b) was obtained for C=O stretching frequency of –COOH group, aromatic ring, and C-O-C stretching frequency. Region (c) was formed mainly due to the bending vibrations.

The result showed that the admissible change in the vibrational frequency was observed mainly in region (a) and region (b) suggesting the participation of the –COOH group along with the benzene ring of the sinapic acid towards the complexation with $NiSO_4$. The peak observed at 3383 cm^{-1} and 3311 cm^{-1} in the pure sinapic acid was shifted and developed a higher intense peak at 3425 cm^{-1} in the nano particles. The peaks in the range of 3021 cm^{-1}-2837 cm^{-1} were also modified due to the formation of NPs. The conjugated carbonyl peak at 1663 cm^{-1} coming from the –COOH of the pure sinapic acid was diminished upon formation of the nanoparticle. The intensity of the peaks in the range 1594 cm^{-1} -1433 cm^{-1} was also modified in presence of $NiSO_4$ solution. The peaks due to –CH_3 bending and –C-O-C- stretching either disappeared or their intensities diminished due to the interaction between the $NiSO_4$ and sinapic acid. The region (c) was also modified upon nanoparticle formation. Table 4.1 shows the results of individual bond vibrations with their possible functionalities [Kumar et al., 2013].

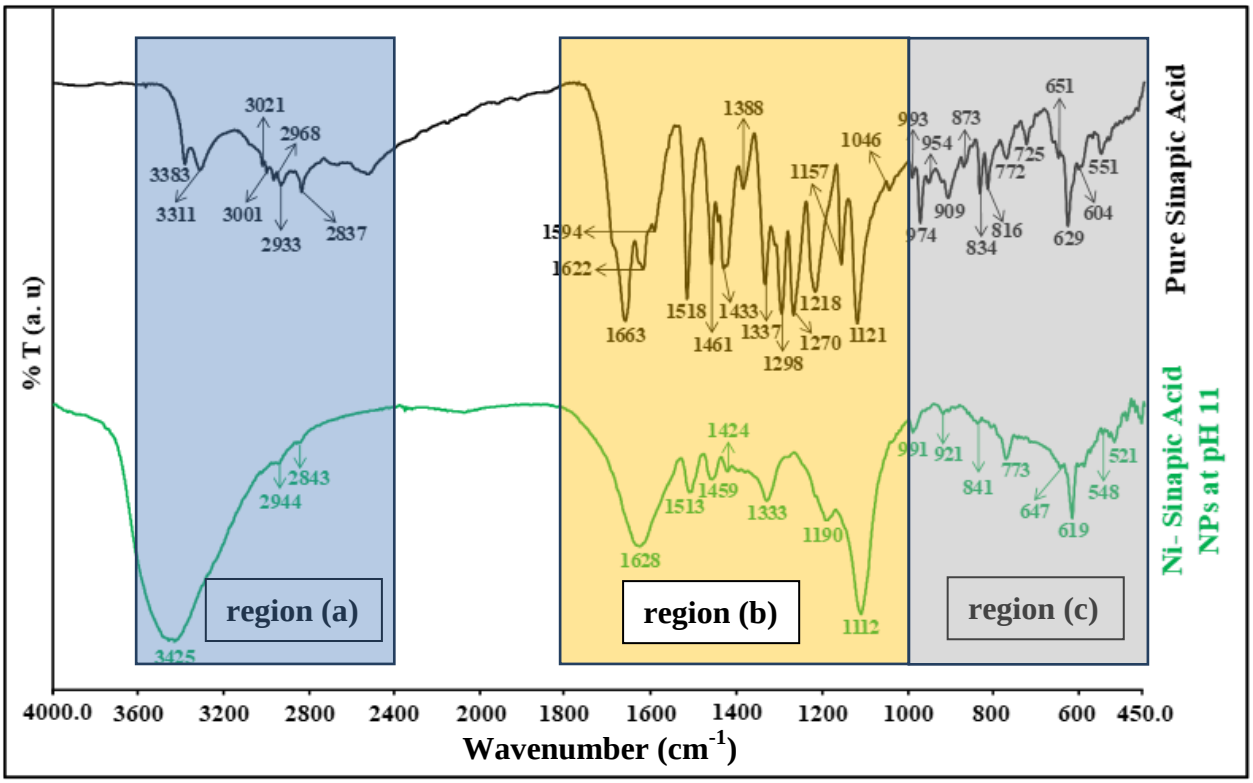

Figure 4.3. FTIR spectra of pure sinapic acid and Ni-SA NPs

Table 4.1. FTIR spectral data of pure sinapic acid and synthesized Ni-SA NPs, along with their potential functionalities

Sample	Peak Position (cm^{-1})	Functionality
Sinapic acid	3383	H-bonded -OH stretching frequency
	3311	
	3021	C-H stretching frequency $-CH_3$ group
	3001	
	2968	
	2933	
	2837	
	1663	C=O stretching frequency of –COOH group
	1622	Aliphatic C=C group stretching
	1594	Aromatic C=C stretching frequency
	1518	

	1461	
	1433	
	1388	-CH_3 bending
	1337	
	1298	
	1270	C-O-C stretching frequency
	1218	
	1157	
	1121	
	1046	
	993	Double bond C-H bending
	974	
	954	
	909	
	873	
	834	Out of plane C-H bending
	816	
	772	
	725	C-H deformation
	651	
	629	
	604	
	551	C-H deformation
Ni_SA NPs	3425	H-bonded -OH stretching frequency
	2944	C-H stretching frequency –CH_3 group
	2843	
	1628	Aliphatic C=C group stretching
	1513	Aromatic C=C stretching frequency
	1459	
	1424	
	1333	-CH_3 bending

	1190	C-O-C stretching frequency
	1112	
	991	Double bond C-H bending
	921	
	841	
	773	Out of plane C-H bending
	647	
	619	
	548	C-H deformation
	521	Ni-O stretching frequency

4.4.4. TEM analysis

The nano dimension of the Ni-SA NPs was confirmed from the TEM images of the NPs (Fig. 4.4a and 4.4b). The particle size was around 5 to 10 nm with intermittent pores. Clear lattice fringes were observed from a slightly zoomed in TEM image suggesting the nano crystallinity of the NPs (Fig. 4.4b). Fig. 4.4c shows the histogram for particle size distribution of the NPs with maximum number of particles having 7 nm sizes. The selected area electron diffraction (SAED) pattern of the NPs showed concentric rings again confirming the nano crystallinity of the NPs (Fig. 4.4d). The spots arose due to the diffraction from (231), (310), (049), (2210), (703) and $(12\bar{6})$ planes which are shown in the SAED pattern.

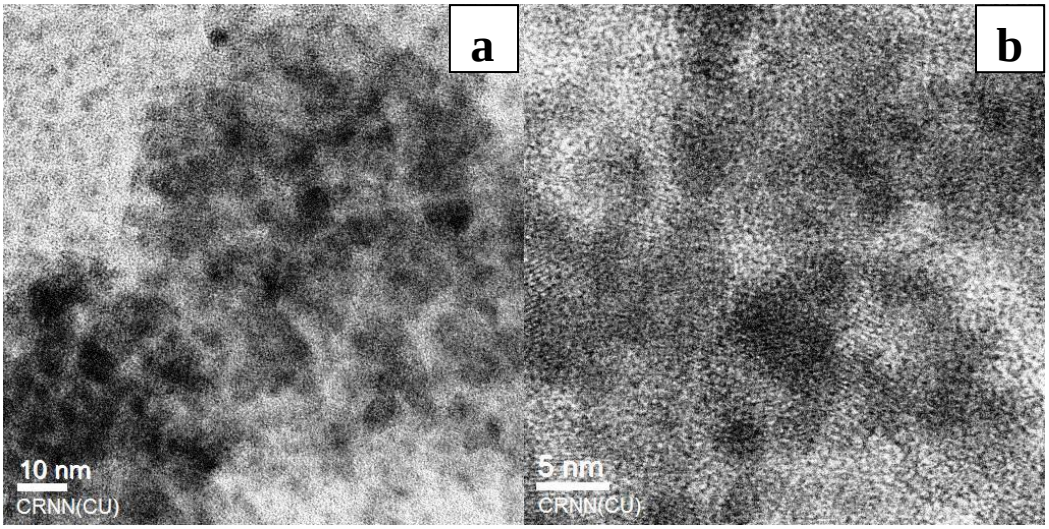

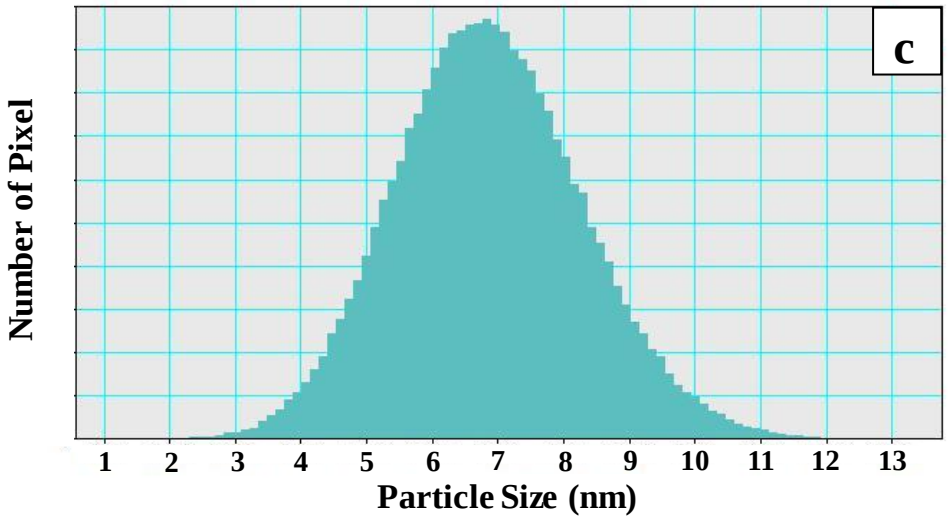

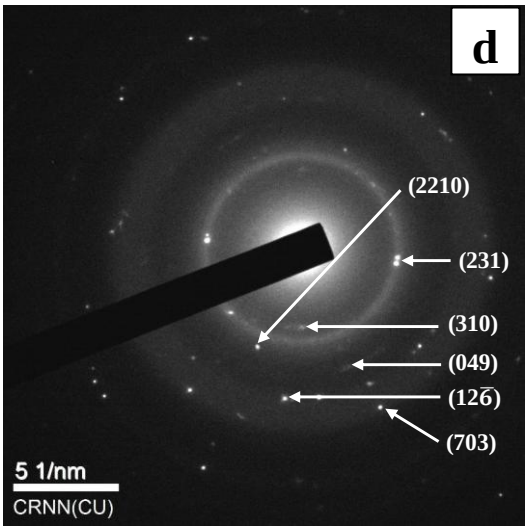

Figure 4.4. (a) and (b) represent the TEM images of Ni-SA NPs and (c) histogram showing particle size distribution of Ni-SA NPs (d) SAED pattern of the Ni-SA NPs

4.4.5. PXRD analysis

The obtained PXRD (Fig.4.5) data were then compared with the unique number from the Joint Committee on Powder Diffraction Standards (JCPDS) (Table 4.3). For Ni-SA NPs, the major diffractions came from 2θ values 23.024°, 33.886º and 60.164° which correspond to ($\bar{2}$11), (310) and ($\bar{1}$15) and ($\bar{3}$22) planes respectively. The PXRD data suggested that the possible crystallographic systems are monoclinic, tetragonal, anorthic and cubic with majority of them having primitive lattice. The obtained PXRD pattern is similar to the β-phase of $Ni(OH)_2$ [El-Kemary et al., 2013; Hall et al., 2015]. The presence of Ni as $Ni(OH)_2$ was further verified from the XPS data discussed later.

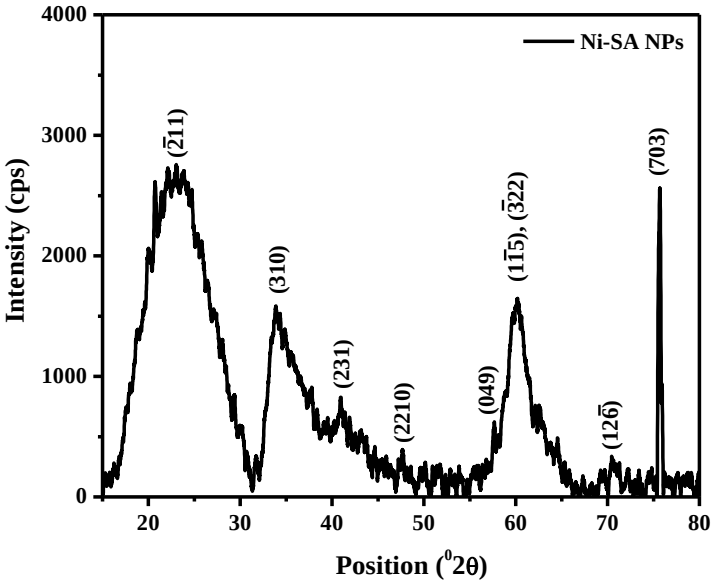

Figure 4.5. PXRD pattern of the Ni-SA NPs

Table 4.2. PXRD data of the prepared nanoparticle and possible assignment of JCPDS no.

Obtained value [°2θ]	Actual Value [°2θ]	Possible hkl plane	Possible System	Possible Lattice	JCPDS No.
23.024	22.101	($\bar{2}$11)	Monoclinic	Body-centered	24-1840
33.886	33.824	(310)	Cubic	Body-centered	15-0782
40.950	40.954	(231)	Anorthic	Primitive	52-2421
47.672	47.664	(2210)	Tetragonal	Primitive	51-2491
57.649	57.658	(049)	Tetragonal	Primitive	51-2491
60.164	60.164	(1$\bar{1}$5), ($\bar{3}$22)	Anorthic	Primitive	51-2104
70.475	70.375	(12$\bar{6}$)	Monoclinic	Primitive	53-1561
75.685	75.583	(703)	Monoclinic	Body-centered	24-1840

4.4.6. XPS analysis

XPS analysis of the Ni-SA NPs reveals the presence of C, O, N and Ni, the total concentrations of which are given in the Table 4.3 and confirms the presence of SA with the Ni NPs. The atomic percentage of C, O, N and Ni are 66.30%, 29.30%, 0.50% and 3.90% respectively.

The binding energy of the Ni($2p_{3/2}$) peak is found at 856.30 eV, which we attribute to $Ni(OH)_2$. Whilst this value is approximately 1 eV higher than that observed for bulk $Ni(OH)_2$ [Biesinger et al., 2009], it is consistent with many examples reported in the NIST (National Institute of Standards and Technology) XPS database [Naumkin et al., 2012]. It is also well established that both electronic and particle size effects can influence the observed binding energy [Ascarelli et al., 1977], with nanoparticulate materials often having higher than expected binding energies [Tao et al., 2008]. Furthermore, the Ni(2p) spectrum (Fig. 4.6) exhibits a spectral envelope broadly consistent with that of $Ni(OH)_2$ which supports this attribution and the Ni-O frequencies observed in the FTIR analysis. It is likely that NiOOH species are also present based on the spectral envelope, however whilst fitting the data using published models [Tao et al., 2008] did not yield a satisfactory fit, we do not exclude some small amount being present.

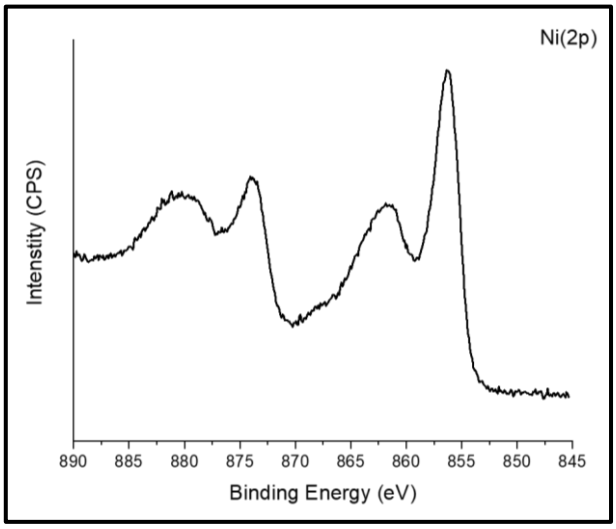

Figure 4.6. Ni(2p) core-level spectrum from the Ni-SA NPs

Table 4.3. Atomic percentage of C, O, N and Ni in Ni-SA NPs as obtained from XPS

Sample	Elemental Concentration (atomic %)			
	C	O	N	Ni
Ni-SA NPs	66.30	29.30	0.50	3.90

4.4.7. Sensing

The sensing study was carried out using absorption spectroscopy. There was no spectral change observed for any of the analytes except permanganate ions. Gradual addition of very small aliquots of permanganate ions, results in the formation of a new peak at 603 nm and decrease of characteristic absorption peak of the Ni-SA NPs (298 nm) (Fig. 4.7).The increase in absorption at 603 nm was observed up to 2 µM concentration of the analyte which symbolizes the interaction between Ni-SA NPs with the permanganate ion and the decrease in the absorption peak at 298 nm was due to dilution of the nano particle solution in presence of minute amount of analyte. The limit of detection is 413 nM and the linear range for this detection is 1.25 to 1.70 µM with correlation coefficient of 0.95. The different analytical parameters for the detection of the $KMnO_4$ ion is tabulated in Table 4.4.

No spectral change was observed for all the other analytes and the respective UV-Vis spectra are presented in the Fig. 4.8. (A-M). The selectivity of the Ni-SA NPs towards the permanganate ion is represented in Fig. 4.9.

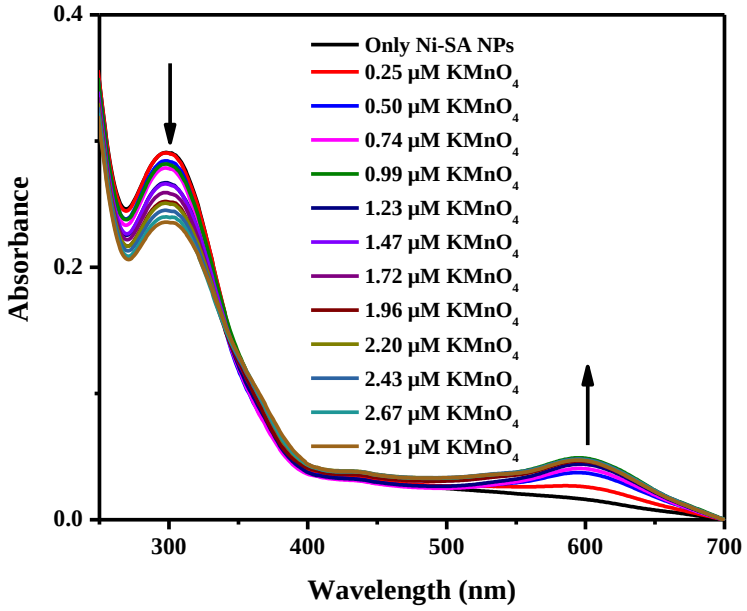

Figure 4.7. Spectral change of nano particle solution in presence of permanganate ion (0-3 µM)

Table 4.4. Different analytical parameters for the detection of the $KMnO_4$

Parameter	Data
Regression equation	Y = sX+C
Slope (s) (μM^{-1})	0.008
Intercept (C)	0.034
Correlation coefficient (R^2)	0.947
Standard deviation (σ)	0.001
Limit of detection (LOD = 3.3× σ/s) (μM)	0.41
Limit of quantification (LOQ = 10× σ/s) (μM)	1.25
Linear range (μM)	1.25 to 1.70
λ (nm)	603

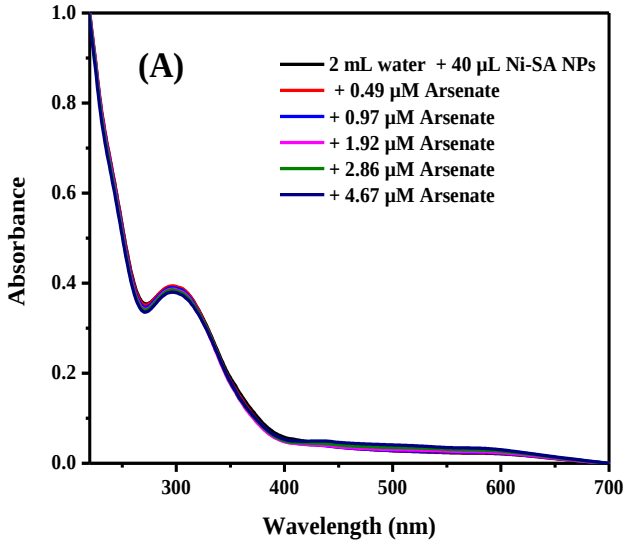

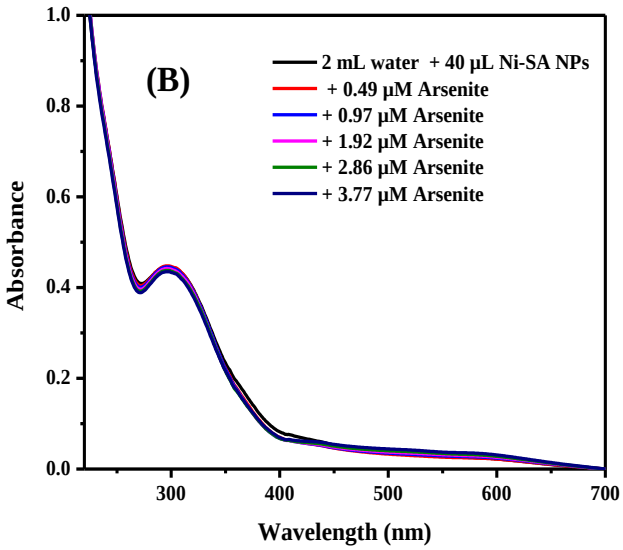

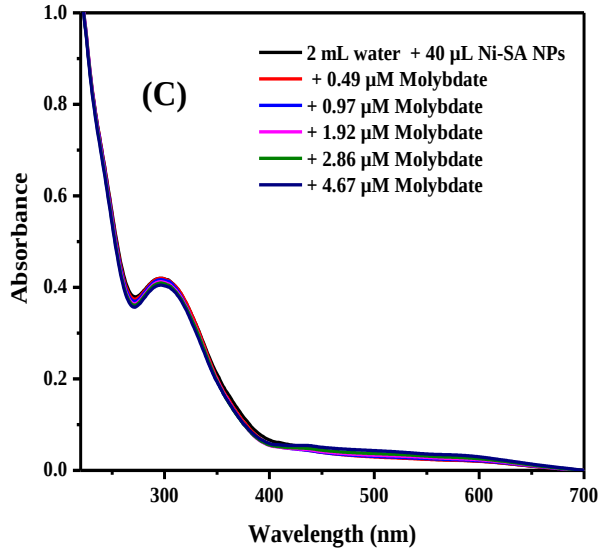
(C)
2 mL water + 40 µL Ni-SA NPs
+ 0.49 µM Molybdate
+ 0.97 µM Molybdate
+ 1.92 µM Molybdate
+ 2.86 µM Molybdate
+ 4.67 µM Molybdate
Absorbance
Wavelength (nm)

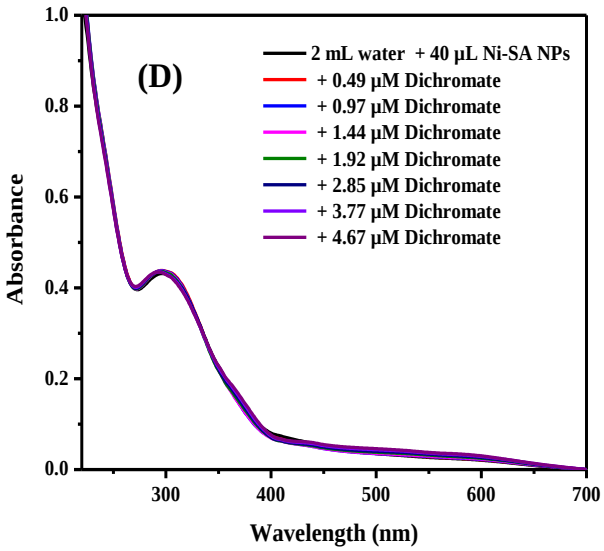
(D)
2 mL water + 40 µL Ni-SA NPs
+ 0.49 µM Dichromate
+ 0.97 µM Dichromate
+ 1.44 µM Dichromate
+ 1.92 µM Dichromate
+ 2.85 µM Dichromate
+ 3.77 µM Dichromate
+ 4.67 µM Dichromate
Absorbance
Wavelength (nm)

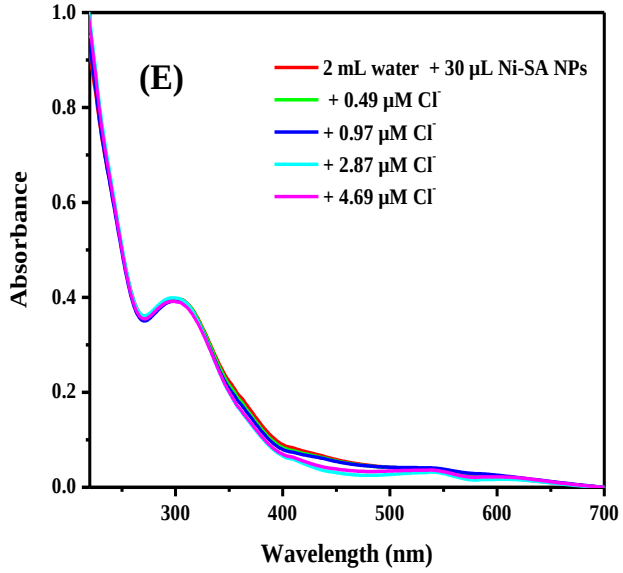
(E)
2 mL water + 30 µL Ni-SA NPs
+ 0.49 µM Cl-
+ 0.97 µM Cl-
+ 2.87 µM Cl-
+ 4.69 µM Cl-
Absorbance
Wavelength (nm)

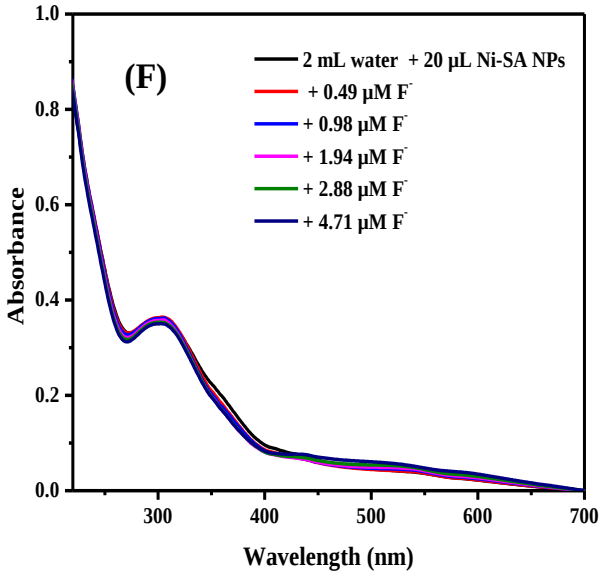
(F)
2 mL water + 20 µL Ni-SA NPs
+ 0.49 µM F-
+ 0.98 µM F-
+ 1.94 µM F-
+ 2.88 µM F-
+ 4.71 µM F-
Absorbance
Wavelength (nm)

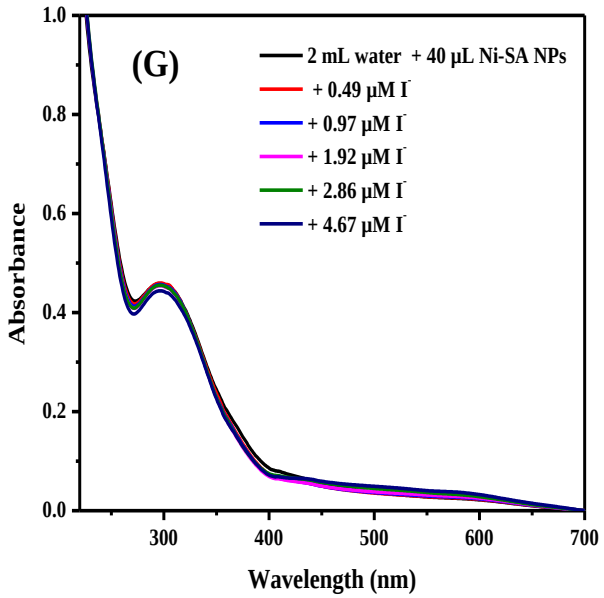
(G)
2 mL water + 40 µL Ni-SA NPs
+ 0.49 µM I-
+ 0.97 µM I-
+ 1.92 µM I-
+ 2.86 µM I-
+ 4.67 µM I-
Absorbance
Wavelength (nm)

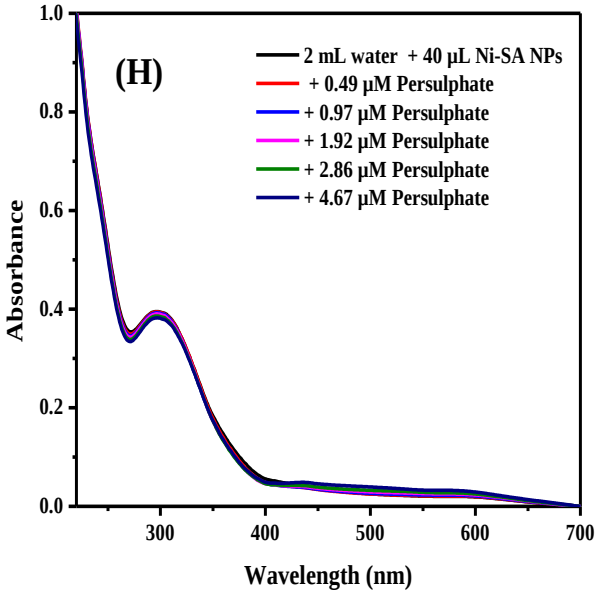
(H)
2 mL water + 40 µL Ni-SA NPs
+ 0.49 µM Persulphate
+ 0.97 µM Persulphate
+ 1.92 µM Persulphate
+ 2.86 µM Persulphate
+ 4.67 µM Persulphate
Absorbance
Wavelength (nm)

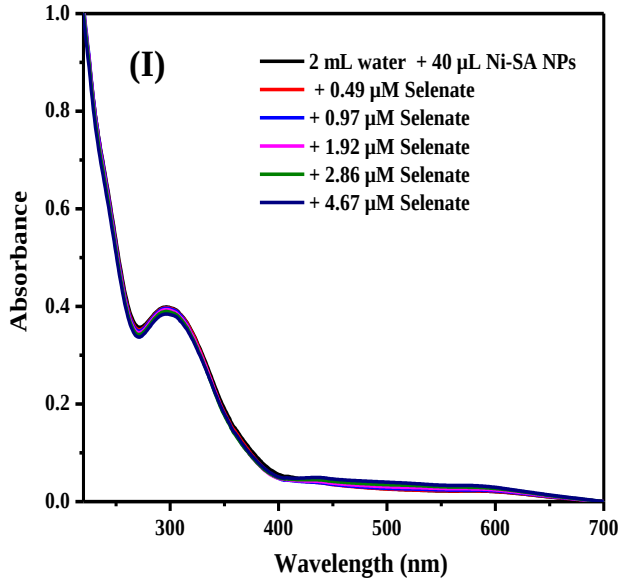
(I)
2 mL water + 40 µL Ni-SA NPs
+ 0.49 µM Selenate
+ 0.97 µM Selenate
+ 1.92 µM Selenate
+ 2.86 µM Selenate
+ 4.67 µM Selenate
Absorbance
Wavelength (nm)

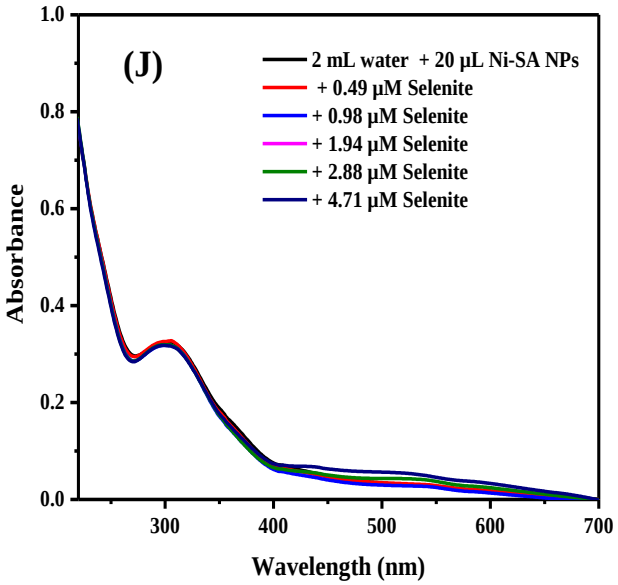
(J)
2 mL water + 20 µL Ni-SA NPs
+ 0.49 µM Selenite
+ 0.98 µM Selenite
+ 1.94 µM Selenite
+ 2.88 µM Selenite
+ 4.71 µM Selenite
Absorbance
Wavelength (nm)

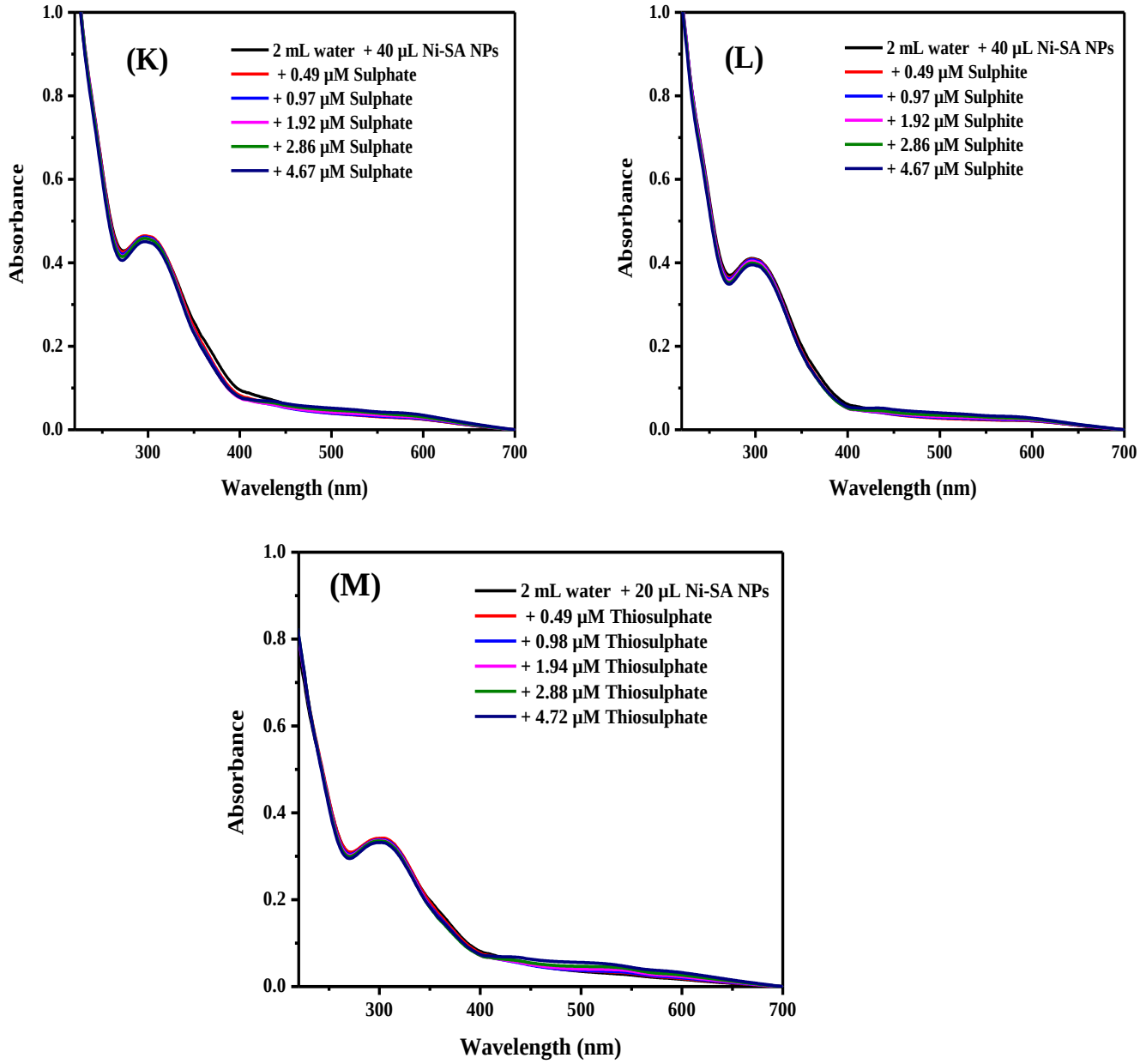

Figure 4.8. Spectral change of Ni-SA NPs upon addition of respective ions, **(A)** arsenate ion (0 to 4.67 µM) **(B)** arsenite ion (0 to 3.77 µM) **(C)** molybdate ion (0 to 4.67 µM) **(D)** dichromate ion (0 to 4.67 µM) **(E)** chloride ion (0 to 4.69 µM) **(F)** fluoride ion (0 to 4.71 µM) **(G)** iodide ion (0 to 4.67 µM) **(H)** persulphate ion (0 to 4.67 µM) **(I)** selenate ion (0 to 4.67 µM) **(J)** selenite ion (0 to 4.71 µM) **(K)** sulphate ion (0 to 4.67 µM) **(L)** sulphite ion (0 to 4.67 µM) **(M)** thiosulphate ion (0 to 4.72 µM)

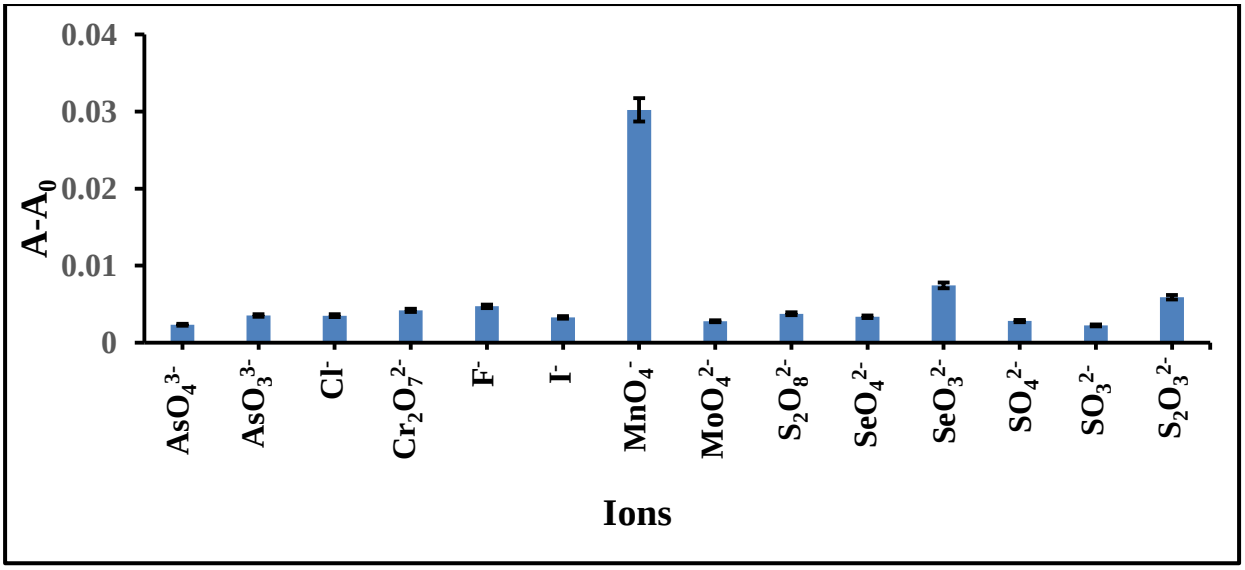

Figure 4.9. Selectivity of the Ni-SA NPs towards permanganate ion

4.4.8. Sensing Mechanism

The sensing mechanism was studied using two different techniques viz., ITC and XPS analysis.

4.4.8.1. ITC analysis

ITC was used to investigate the sensing mechanism and obtain a comprehensive picture of the thermodynamic parameters for the interaction of $KMnO_4$ with the NPs. At 298 K, the interaction between $KMnO_4$ with the NPs was investigated in aqueous medium. The stoichiometry of interaction between $KMnO_4$ with the NPs was found to be 1:1, with an association constant (K_a) of 1.54×10^4 M^{-1} (Fig. 4.10). The changes in enthalpy (ΔH) and entropy (ΔS) associated with this interaction are -80 kcal/mol and -2.97 kcal/mol/deg, respectively. The ΔG value obtained from the experiment is -5.72 kcal/mol.

Therefore, the interaction process between $KMnO_4$ with the NPs appears to be an enthalpy driven process.

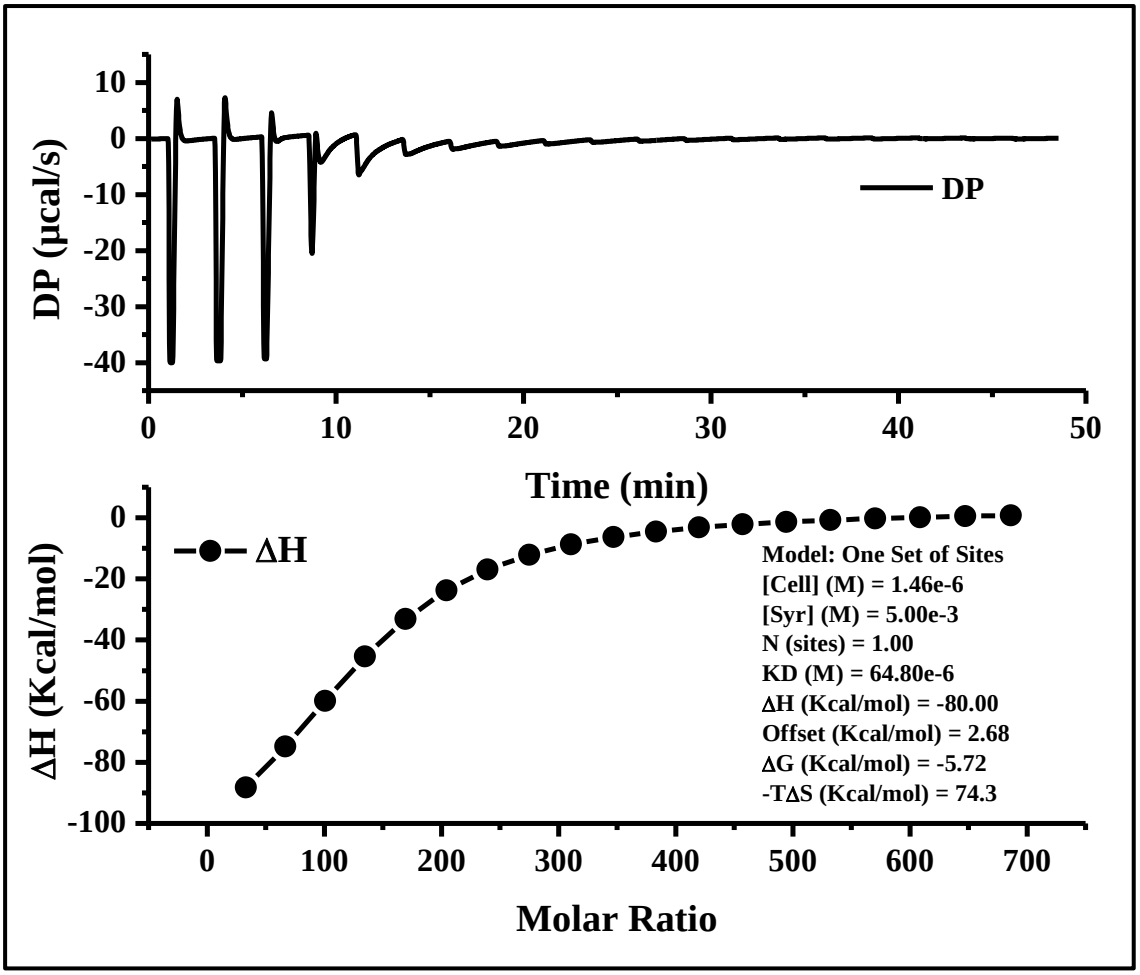

Figure 4.10. ITC data for binding isotherm between $KMnO_4$ with the NPs at 298 K

4.4.8.2. XPS analysis

Analysis of the permanganate treated sample revealed the presence of K and Mn in addition to the C, O and Ni previously noted for the Ni-SA NPs. The Ni($2p_{3/2}$) binding energy here is found to be 855.4 eV (Fig. 4.11(a)), almost 1 eV lower than Ni-SA NPs sample. Whilst remaining in the Ni(II) oxidation state, the shift downward in energy is accompanied by a change in the spectral envelope with a somewhat sharper signal in the satellite structure above 860 eV (Fig. 4.11(b)). The binding energy of 855.4 eV is broadly consistent with that of bulk $Ni(OH)_2$ and NiOOH species, with the sharper satellite structure likely indicative of a greater hydroxide content.

Analysis of the Mn($2p_{3/2}$) signal (not shown) is slightly complicated by its superposition on the Ni Auger. Nevertheless, a broad asymmetric peak centred at 642.5 eV is observed. This binding energy is significantly lower than $KMnO_4$ (645.5 eV), so cannot be ascribed solely to the permanganate, an observation which is confirmed by the relative percentages of K and Mn in the atomic % table (Table 4.6). The atomic percentage of C, O, Ni, K and Mn are 22.4

%, 47.2 %, 5.4 %, 4.3 % and 20.8 % respectively. Analysis of the spectral envelope shows no sharp peak structure associated with MnO_2, and hence we attribute the Mn speciation to be Mn_2O_3 and/or MnOOH based on the data envelope alone [Biesinger et al., 2011].

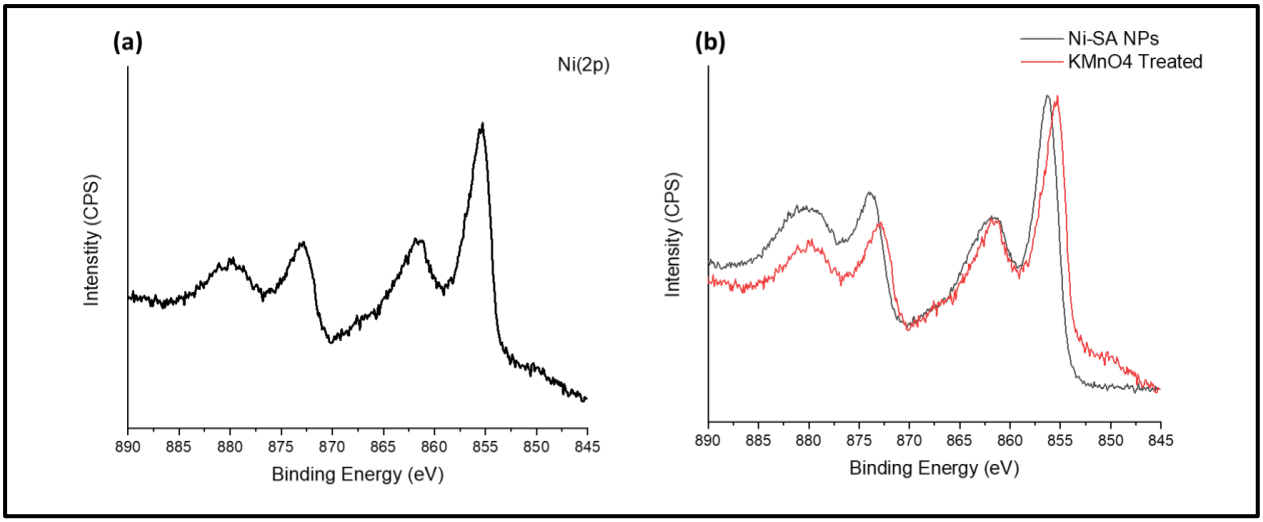

Figure 4.11. (a) Ni(2p) core-level spectrum from the $KMnO_4$ treated Ni-SA NPs (a) and (b) normalised overlay of the Ni(2p) spectra from the two materials

Upon treatment with $KMnO_4$, the organic part containing SA was found to become oxidized by the MnO_4^- ion. The amount of inorganic Ni content increased while the C content was found to decrease. The atomic percentage of O was increased due to the simultaneous oxidation of the organic sphere and the presence of Mn as Mn_2O_3 and/or MnOOH (Table 4.3 and 4.5).

Table 4.5. Atomic percentage (at %) of C, O, Ni, K and Mn in $KMnO_4$ treated Ni-SA NPs as obtained from XPS

Sample	Elemental Concentration (atomic %)				
	C	O	Ni	K	Mn
$KMnO_4$ treated Ni-SA NPs	22.40	47.20	5.40	4.30	20.80

Overall, the mechanism can be summarised as an oxidation of the organic sphere attached to the Ni(II) of Ni-SA by the permanganate ions which itself gets reduced from Mn(VII) to

Mn(III). Mn remains in the system as Mn_2O_3 and/or MnOOH as has been revealed by XPS. Reduction of Mn(VII) to Mn(III) occurs in neutral medium as can be observed from the experimental findings which also agrees with previous reports [Gao et al., 2017; Ahmed, 2016]. The absorption spectral sensing (Fig. 4.7) shows appearance of the new peak at 603 nm which gradually increases with increasing permanganate concentration. This appears due to $n \rightarrow \pi^*$ transition of unshared electrons of O present in Mn_2O_3 to one of the antibonding orbitals of the oxidized organic sphere. The intensity of the peak grows with increasing population of 'n' which again is dependent on the concentration of the added analyte (permanganate, which gets reduced to yield Mn_2O_3).

4.4.9. Interference

The interference experiment was carried out in the presence of other cations and anions at the same concentration as that of MnO_4^- ion. The obtained results (Fig. 4.12) indicated that there was no significant interference from any of the ions in the detection of trace amounts of MnO_4^- ion. Hence, this process offers a high selectivity for sensing of MnO_4^- ion in the presence of other co-existing cations and anions.

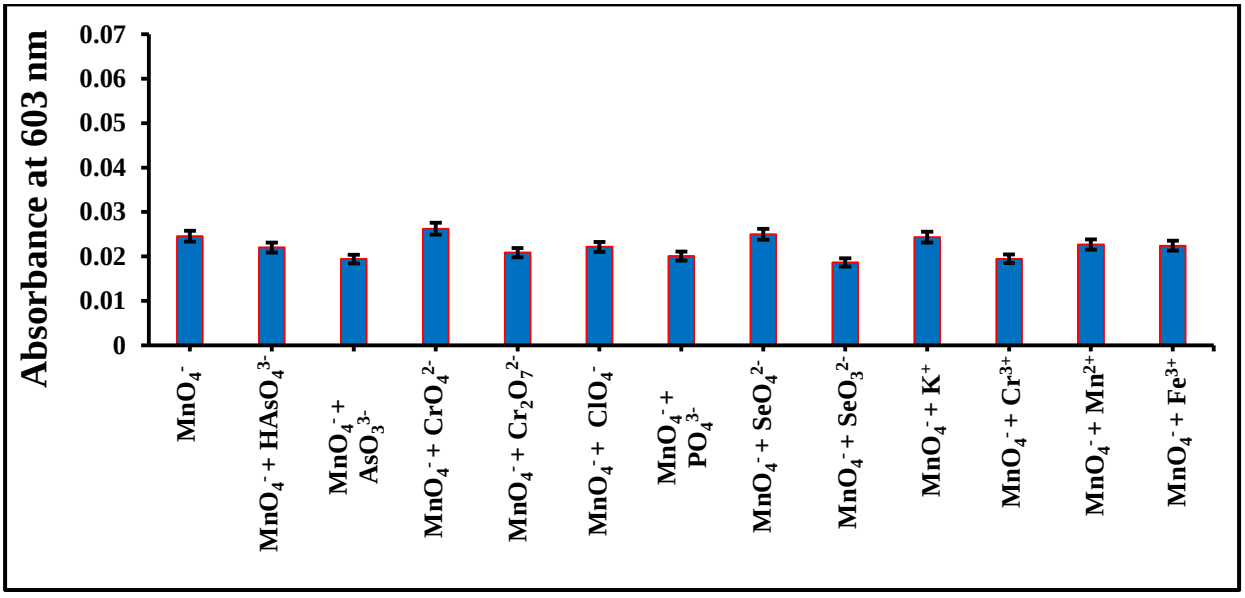

Figure 4.12. Interference study for the sensing of permanganate ion

4.4.10. Analysis of natural samples

Practicability of the present technique has been examined upon analyses of the natural samples. The analyses suggested that, all the studied samples have permanganate contamination and this has been proved using the current methodology. The maximum contamination was obtained for the water sample from Sonarpur area (256.25 µM). The water

sample from Garia also contains measurable amount of $KMnO_4$ (94.88 µM). The source of this contamination may have come from the water treatment done using $KMnO_4$ at the reservoir of the water. The colour of the sweet potato in most of the cases is due to the addition of $KMnO_4$ and other contaminants. The extract of sweet potato was in fact found to contain $KMnO_4$ in a measurable amount (~154 µM). The tap water collected from Rajabazar area did not show any measurable amount of $KMnO_4$.

The spectral changes were instantaneous and the spectra remained unaffected with longer incubation times. Each experiment was repeated for three consecutive times and the precision of the results is reflected standard deviation shown in the table. The recovery percentage of $KMnO_4$ from tap water was also examined and the results (Table 4.6) show that ~88 to 108 % of the added $KMnO_4$ could be recovered. Hence the methodology can be equally applicable towards the environmental samples.

Table 4.6. Recovery percentage of $KMnO_4$ in tap water

Added (µM)	Found (µM)	Recovery (%)
0.49	0.43 (± 0.02)	88 (± 4.10)
0.97	1.00 (± 0.05)	103 (± 5.05)
1.44	1.43 (± 0.07)	99 (± 5.00)
2.86	3.00 (± 0.15)	105 (± 5.13)
3.32	3.57 (± 0.18)	107 (± 5.45)
3.77	3.86 (± 0.19)	102 (± 5.40)

4.5. Conclusion

The Ni-SA NPs material is a suitable candidate for a simple cost effective absorption based spectrophotometric sensing of MnO_4^- ions. The method of synthesis of the nanoparticles is also simple and environment friendly as the polyphenolic acid chosen for nano-synthesis is nature derived. Moreover, the methodology is also hazard free. The prepared NPs can sense MnO_4^- ions at micromolar range (µM) and the sensing technique involves no interference from contemporary ions. The enthalpy driven interaction between Ni-SA NPs and the

$KMnO_4$ was further studied using XPS analysis. The atomic percentage of different atoms including Ni (II) was varied in presence of the MnO_4^- ion. The organic compound (SA) was found to get affected upon permanganate treatment, which was ascertained from the XPS analysis. However, a short linear dynamic range is a drawback of the present method which may be overcome by judicious sample dilution. Applicability of the present technique has also been studied towards natural water samples and in vegetable. Around 88 to 108% of $KMnO_4$ could be recovered from natural sample. The technique and limit of detection of the present method has been compared with the literature and is found to be at per even after using solvent free conditions and sample instrumentations [Liu et al., 2019].

4.6. References

Ahmed, K.A.M., 2016. Exploitation of $KMnO_4$ material as precursors for the fabrication of manganese oxide nanomaterials. Journal of Taibah University for Science. 10, 412-429.

Anandan, B., Rajendran, V., 2011. Morphological and size effects of NiO nanoparticles via solvothermal process and their optical properties. Materials Science in Semiconductor Processing. 14, 43-47.

Ascarelli, P., Cini, M., Missoni, G., Nistico, N., 1977. XPS line broadening in small metal particles. Le Journal de Physique Colloques. 38, C2-125.

Beach, E.R., Shqau, K., Brown, S.E., Rozeveld, S.J., Morris, P.A., 2009. Solvothermal synthesis of crystalline nickel oxide nanoparticles. Materials Chemistry and Physics. 115, 371-377.

Bhattacharyya, S., Rana, D., Bhattacharyya, S.N., 1997. Determination of heat of formation of associated systems by calorimetry. Journal of the Indian Chemical Society. 74, 103-107.

Bhattacharyya, S., Rana, D., Bhattacharyya, S.N., 1997. A thermodynamic study of molecular association by gas liquid chromatography, Journal of the Indian Chemical Society. 74, 456-463.

Bhattacharyya, S., Rana, D., Bhattacharyya, S.N., 1997. A thermodynamic study of molecular association by gas-liquid chromatography: Trilaurylaminealcohol systems. Journal of the Indian Chemical Society. 74, 548-551.

Biesinger, M.C., Payne, B.P., Grosvenor, A.P., Lau, L.W., Gerson, A.R., Smart, R.S.C., 2011. Resolving surface chemical states in XPS analysis of first row transition metals, oxides and hydroxides: Cr, Mn, Fe, Co and Ni. Applied Surface Science. 257, 2717-2730.

Biesinger, M.C., Payne, B.P., Lau, L.W., Gerson, A., Smart, R.S.C., 2009. X-ray photoelectron spectroscopic chemical state quantification of mixed nickel metal, oxide and hydroxide systems. Surface and Interface Analysis. 41, 324-332.

Chandra, S., Kumar, A., Tomar, P.K., 2014. Synthesis of Ni nanoparticles and their characterizations. Journal of Saudi Chemical Society. 18, 437-442.

El-Kemary, M., Nagy, N., El-Mehasseb, I., 2013. Nickel oxide nanoparticles: synthesis and spectral studies of interactions with glucose. Materials Science in Semiconductor Processing. 16, 1747-1752.

Ezhilarasi, A.A., Vijaya, J.J., Kaviyarasu, K., Zhang, X., Kennedy, L.J., 2020. Green synthesis of nickel oxide nanoparticles using solanum trilobatum extract for cytotoxicity,

antibacterial and photocatalytic studies. Surfaces and Interfaces. 20, 100553-100570.

Fairley, N., Fernandez, V., Richard-Plouet, M., Guillot-Deudon, C., Walton, J., Smith, E., Flahaut, D., Greiner, M., Biesinger, M., Tougaard, S., Morgan, D., 2021. Systematic and collaborative approach to problem solving using X-ray photoelectron spectroscopy. Applied Surface Science Advances. 5, 100112-100125.

Gao, Y., Jiang, J., Zhou, Y., Pang, S.Y., Ma, J., Jiang, C., Wang, Z., Wang, P.X., Wang, L.H., Li, J., 2017. Unrecognized role of bisulfite as Mn (III) stabilizing agent in activating permanganate (Mn (VII)) for enhanced degradation of organic contaminants. Chemical Engineering Journal. 327, 418-422.

Gebretinsae, H.G., Tsegay, M.G., Nuru, Z.Y., 2021. Biosynthesis of nickel oxide (NiO) nanoparticles from cactus plant extract. Materials Today: Proceedings. 36, 566-570.

Golovin, Y.I., Golovin, D.Y., Shuklinov, A.V., Stolyarov, R.A., Vasyukov, V.M., 2011. Electrodeposition of nickel nanoparticles onto multiwalled carbon nanotubes. Technical Physics Letters. 37, 253-255.

Halder, M., Islam, M.M., Singh, P., Singha Roy, A., Islam, S.M., Sen, K., 2018. Sustainable generation of $Ni(OH)_2$ nanoparticles for the green synthesis of 5-substituted 1 H-tetrazoles: a competent turn on fluorescence sensing of H_2O_2. ACS Omega. 3, 8169-8180.

Hall, D.S., Lockwood, D.J., Bock, C., MacDougall, B.R., 2015. Nickel hydroxides and related materials: a review of their structures, synthesis and properties. Proceedings of the Royal Society A: Mathematical, Physical and Engineering Sciences. 471, 20140792-20140810.

Hemalatha, M., Suryanarayanan, N., Prabahar, S., 2014. Synthesis and characterization of nickel nanoparticles by chemical reduction method. Optoelectronics and Advanced Materials-Rapid Communications. 8, 288-291.

Kumar, N., Fuloria, F., 2013. Spectroscopy: fundamentals and data interpretation. Studium Press. 253-255.

Lin, T.W., Huang, S.D., 2001. Direct and simultaneous determination of copper, chromium, aluminum, and manganese in urine with a multielement graphite furnace atomic absorption spectrometer. Analytical Chemistry. 73, 4319-4325.

Liu, H., Rong, J., Shen, G., Song, Y., Gu, W., Liu, X., 2019. A fluorescent probe for sequential sensing of MnO_4^- and $Cr_2O_7^{2-}$ ions in aqueous medium based on a UCNS/TMB nanosystem. Dalton Transactions. 48, 4168-4175.

Lemos, V.A., Novaes, C.G., Bezerra, M.A., 2009. An automated preconcentration system for the determination of manganese in food samples. Journal of Food Composition and

Analysis. 22, 337-342.

Ma, Y., Zhang, G., Pan, J., 2012. Spectroscopic studies of DNA interactions with food colorant indigo carmine with the use of ethidium bromide as a fluorescence probe. Journal of Agricultural and Food Chemistry. 60, 10867-10875.

Madhumitha, G., Elango, G., Roopan, S.M., 2016. Biotechnological aspects of ZnO nanoparticles: overview on synthesis and its applications. Applied Microbiology and Biotechnology. 100, 571-581.

Mati, S.S., Roy, S.S., Chall, S., Bhattacharya, S., Bhattacharya, S.C., 2013. Unveiling the groove binding mechanism of a biocompatible naphthalimide-based organoselenocyanate with calf thymus DNA: an "ex vivo" fluorescence imaging application appended by biophysical experiments and molecular docking simulations. The Journal of Physical Chemistry B. 117, 14655-14665.

Mohammadijoo, M., Khorshidi, Z.N., Sadrnezhaad, S.K., Mazinani, V., 2014. Synthesis and characterization of nickel oxide nanoparticle with wide band gap energy prepared via thermochemical processing. Nanoscience and Nanotechnology: An International Journal. 4, 6-9.

Montomery, J.J., 1985.Water treatment: principles and design, principles and design. John Wiley & Sons. 553-580.

Naumkin, A.V., Kraut-Vass, A., Gaarenstroom, S.W., Powell, C.J., 2012. NIST X-ray photoelectron spectroscopy database, version 4.1. National Institute of Standards and Technology: Gaithersburg. 870-890.

Paul, B.K., Guchhait, N., 2011. Exploring the strength, mode, dynamics, and kinetics of binding interaction of a cationic biological photosensitizer with DNA: implication on dissociation of the drug-DNA complex via detergent sequestration. The Journal of Physical Chemistry B. 115, 11938-11949.

Petit, C.T., Alsulaiman, M.S., Lan, R., Tao, S., 2012. Direct synthesis of Ni nanoparticles by a non-aqueous sol-gel process. Nanoscience and Nanotechnology Letters. 4, 136-141.

Qamar, M., Gondal, M.A., Yamani, Z.H., 2011. Synthesis of nanostructured NiO and its application in laser-induced photocatalytic reduction of Cr (VI) from water. Journal of Molecular Catalysis A: Chemical. 341, 83-88.

Ramirez-Meneses, E., Torres-Huerta, A.M., Dominguez-Crespo, M.A., Ponce-Varela, M.G., Hernandez-Perez, M.A., Betancourt, I., Palacios-Gonzalez, E., 2014. Synthesis and electrochemical characterization of Ni nanoparticles by hydrazine reduction using hydroxyethyl cellulose as capping agent. Electrochimica Acta. 127, 228-238.

Sabouri, Z., Akbari, A., Hosseini, H.A., Darroudi, M., 2018. Facile green synthesis of NiO nanoparticles and investigation of dye degradation and cytotoxicity effects. Journal of Molecular Structure. 1173, 931-936.

Sathishkumar, P., Gu, F.L., Zhan, Q., Palvannan, T., Yusoff, A.R.M., 2018. Flavonoids mediated 'Green'nanomaterials: a novel nanomedicine system to treat various diseases-current trends and future perspective. Materials Letters. 210, 26-30.

Sengupta, P., Ganguly, A., Bose, A., 2018. A phenolic acid based colourimetric 'naked-eye'chemosensor for the rapid detection of Cu (II) ions. Spectrochimica Acta Part A: Molecular and Biomolecular Spectroscopy. 198, 204-211.

Subramanya, S.H., Pai, V., Bairy, I., Nayak, N., Gokhale, S., Sathian, B., 2018. Potassium permanganate cleansing is an effective sanitary method for the reduction of bacterial bioload on raw coriandrum sativum. BMC Research Notes. 11, 1-5.

Sun, W., Xiao, L., Wu, X., 2019. Facile synthesis of NiO nanocubes for photocatalysts and supercapacitor electrodes. Journal of Alloys and Compounds. 772, 465-471.

Tao, J.G., Pan, J.S., Huan, C.H.A., Zhang, Z., Chai, J.W., Wang, S.J., 2008. Origin of XPS binding energy shifts in Ni clusters and atoms on rutile TiO_2 surfaces. Surface Science. 602, 2769-2773.

Teo, K.C., Chen, J., 2001. Determination of manganese in water samples by flame atomic absorption spectrometry after cloud point extraction. Analyst. 126, 534-537.

Tu, Y.J., Tian, Y.H., Yang, Y.L., 2019. High-sensitivity and selectivity detection of permanganate ions based on pig liver-based carbon quantum dots. Applied Ecology and Environmental Research. 17, 7249-7263.

Wang, H., Jiao, X., Chen, D., 2008. Monodispersed nickel nanoparticles with tunable phase and size: synthesis, characterization, and magnetic properties. The Journal of Physical Chemistry C. 112, 18793-18797.

Wu, J.X., Yan, B., 2017. Eu (III)-functionalized In-MOF (In (OH) bpydc) as fluorescent probe for highly selectively sensing organic small molecules and anions especially for $CHCl_3$ and MnO_4^-. Journal of Colloid and Interface Science. 504, 197-205.

Ye, Z., Weng, R., Ma, Y., Wang, F., Liu, H., Wei, L., Xiao, L., 2018. Label-free, single-particle, colorimetric detection of permanganate by GNPs@ Ag core-shell nanoparticles with dark-field optical microscopy. Analytical Chemistry. 90, 13044-13050.